Tessellation growth models for polycrystalline microstructures

Kirubel Teferra *, Lori Graham-Brady

Dept. of Civil Engineering, Johns Hopkins University, MD, USA

ABSTRACT

This work proposes novel models to represent and parametrize random morphology of polycrystalline microstructures. The reliability of high-fidelity mechanical analysis of polycrystalline microstructures depends upon the morphological representation of the virtual model. Two models addressed in this work are spherical growth and ellipsoidal growth tessellations in which grains grow as spheres (or ellipsoids) with random velocities which initiate from random nucleation sites represented by a spatial point process. All of the stochastic parameters can be represented by a marked point process random field model, for which simulation algorithms exist. Probability distributions of the model parameters are estimated by obtaining best-fit realizations of the models to a data set of a reconstructed microstructure specimen. The accuracy to which these tessellation models can represent real microstructures is evaluated using two example data sets by computing numerous microstructure features as well as the mismatch volume between the best-fit realizations and the data. The spherical growth and ellipsoidal growth tessellations demonstrate very significant improvements over the Voronoi tessellation, while remaining low dimensional representations of the microstructure. Realizations generated from a marked point process random field model show very good agreement in grain size, aspect ratio, and nearest neighbor distributions compared to an example data set. Thus, subsequent realistic instantiations of microstructures having the same statistical characteristics of the data can be trivially obtained, which are necessary to propagate the uncertainty associated with morphological randomness on response quantities of interest in mechanics-based applications.

© 2015 Elsevier B.V. All rights reserved.

1. Introduction

The role that physics-based mechanics models have in identifying the relationships between microstructure and properties (e.g. [13,50]) is increasing due to advancements in experimental characterization and testing, constitutive modeling, computational resources, and simulation algorithms. In order to run high-fidelity mechanical models of metals (e.g. CPFEM) at the microscale, the simulation of statistically equivalent instantiations of random polycrystalline microstructures is a necessary prerequisite. For example, stress and strain localization, dislocation formation, and texture evolution are known to be dependent on polycrystalline configuration, notably crystallographic orientation and grain boundary types and morphology (e.g. [4,25,27,30,37,38,51]). Therefore, quantifying the uncertainty of the predicted responses requires propagating the stochastic properties of microstructure morphology through such models.

The ability to accurately represent material microstructure morphology through parametrized models that can then be

simulated is a challenging and ongoing research topic: there exists a trade off between ease of simulation and complexity of the microstructure representation. Proposed models have ranged from purely probabilistic models that attempt to capture the statistics of morphological features of the final microstructure to physics-based models attempting to simulate phase transformation and recrystallization. Examples of the range of models to represent microstructures include spatial tessellations [35], Monte Carlo Potts models (e.g. [1,43]), Cellular Automata models (e.g. [36,43]), Kolmogorov–Johnson–Mehl–Avrami based approaches (e.g. [10]), the level-set method (e.g. [24]), and phase field models (e.g. [53]). Physics-based models have the ability to generate complex morphological structures that capture features of the final and evolving microstructure, and, more importantly, can model the effects of material processing techniques and plastic deformation on the final microstructure. However, the generation of microstructures through first-principles, physics-based models (e.g. the solution to partial differential equations formulated on thermodynamics, diffusion, and advection processes) can be a very challenging problem in itself. On the other hand, phenomenological models such as Cellular Automata or Monte Carlo Potts models are easier to implement but require optimization of its

control parameters and transformation rules to represent a target microstructure. Purely probabilistic models (i.e. tessellations) offer no insight into materials processing but are the cheapest computationally and easiest to implement in an optimization routine to match target microstructure features. Thus, the choice of the type of model depends on the application of interest.

For problems involving mechanical simulation of the final microstructure, polycrystalline microstructures are typically modeled using random tessellation models [31]. The Voronoi Tessellation (VT) is the most mathematically developed and widely used model in mechanical simulation (e.g. [2,4,5,14,23]). VTs are rather restrictive due to their limited ability to capture variation in grain size distribution and to represent irregularly shaped grains (e.g. oblique and non-convex shapes). Due to the limitations of VTs, other tessellation models have been developed (e.g. Laguerre tessellations [20,28], Johnson–Mehl Tessellation [32], and Voronoi-G tessellations [47]) although few cases involve mechanical analysis (e.g. Laguerre tessellation [39], and the Voronoi-G tessellation [19,34]).

Instead of utilizing mathematically developed random tessellation models, a number of researchers have developed optimization-based methods to generate so-called statistically equivalent microstructures. In these approaches, an objective function based on the difference between statistics of features of the target and the simulated microstructure is minimized. Example methods of these are the algorithm in DREAM.3D software [17], the algorithms from which the MBUILDER package is based [7,45,49], and a similar method in Ref. [52]. A general description of these methodologies is as follows. The distribution of the semi-axes of best-fit ellipsoids to grains of a microstructure reconstructed from experimental data (e.g. EBSD-FIB serial sectioning) is obtained. Ellipsoids are simulated from this distribution and randomly inserted in a spatial domain according to a uniform distribution. The filling-in of empty spaces and removal of overlaps are typically done through a simulating annealing optimization routine that aims to minimize surface energy or some related cost function. The remaining unassigned space is filled by a homogeneous growth of the ellipsoids where their nucleation times is a function of their volume. Then realizations of the crystallographic orientation per grain is determined such that some statistic (e.g. orientation and misorientation distribution function) obtained from EBSD data is matched through another simulated annealing optimization step. This is the base microstructure, and a final step can be included to insert twins [55].

Although these methods represent the current state-of-the-art in generating statistically equivalent polycrystalline microstructures (without resorting to physics-based approaches), there are significant challenges and limitations. The generation of every microstructure involves multiple optimization routines, which can be computationally expensive, especially if multiple virtual microstructures are sought. Furthermore, the multiple steps to obtain the final microstructure obfuscate the relationships between the input parameters and the final microstructure. This makes it difficult to know the range of target distributions that can be captured and how to tune each step to improve the convergence of the optimization routine. Also, it is unclear how these methods can handle potential correlations between morphology and crystallographic texture or spatial correlations without creating a very complex objective function whose minimum may still result in a poor fit.

The purpose of this paper is to demonstrate that parametric tessellation models can be accurate in representing microstructure morphology and also can be easily simulated to generate statistically equivalent microstructures. The models considered are (1) a spherical growth tessellation (also known as multiplicatively weighted tessellation [35, Chpt. 3.1.1]) where nucleation sites are modeled as a spatial point process and each grain grows with its own random velocity until impinging on another grain, and (2) an ellipsoidal growth tessellation which extends from the spherical growth model such that grains grow as ellipsoids with random semi-axis components and orientations. The parameters of the models can be described by the marked point process (MPP) [9,22,33] random field model for which simulation algorithms exist.

In general, it is a challenge to estimate the probability distributions of the parameters. In this work, parameter distributions are obtained by identifying a best-fit realization of the models to a reconstructed microstructure data set by minimizing the mismatch volume between the data and the tessellation model. Thus, a limitation to the approach as presented in the paper is that obtaining the distributions of model parameters, which are then simulated to generate statistically equivalent microstructure samples, requires at least one data set of a reconstructed microstructure. If no microstructure data is available and target statistics are sought, then an inverse problem can be formulated in order to identify the parameter distributions that lead to the target statistics. This is the focus of numerous previous works such as the optimization-based approaches discussed above for polycrystalline materials as well as some examples for composites [15,16,26,56]. A similar strategy can be pursued for the proposed tessellation models although this is beyond the scope of this paper. Therefore the contributions of this paper entail: (1) the introduction of a method to establish best-fit tessellation samples to microstructure data as a means to compare the accuracy of different tessellation models (2) the introduction of the ellipsoidal growth tessellation as a viable forward model to represent polycrystalline morphology, and (3) the introduction of the MPP model having the marks comprising a random vector along with a simulation algorithm to match target marginal distributions and covariance matrices.

The paper is outlined as follows. The definitions of the Voronoi, spherical growth, and ellipsoidal growth tessellations are given (Section 2) followed by how best-fit realizations of such models are obtained from a reconstructed microstructure (Sections 3 and 4) with two examples provided (Section 5). A suitable random field model and simulation algorithm for the one of the example data sets is given in Section 6, which is followed by concluding statements.

2. Microstructure representation with tessellation models

A tessellation $m = \{C_j\}$ is a collection of cells $C_j \subset \mathbb{R}^d : j = 1, 2, \ldots, N_C$ defined as [31]

$$\mathring{C}_j \bigcap \mathring{C}_k = \phi, \tag{1a}$$

$$\bigcup_j C_j = \mathbb{R}^d, \tag{1b}$$

$$\#\{C_j \in m : C_j \cap B \neq \phi\} < \infty \text{ for all bounded } B \subset \mathbb{R}^d, \tag{1c}$$

where Eq. (1a) states that the interior of cells ($\mathring{C}$) do not intersect, Eq. (1b) states the tessellation is spacefilling (i.e. no empty spaces), and Eq. (1c) states that a tessellation is a countable set of cells. Polycrystalline microstructure morphology satisfies the definition of a tessellation for $x \in \mathbb{R}^3$ (e.g. the grains are represented by tessellation cells), and a few models with varying complexity are discussed below.

A 3D Voronoi Tessellation (VT) is defined such that every point in space is assigned to the cell with the nearest nucleation site, and is given by

$$C_j = \{x \in \mathbb{R}^3 : \|x - X_j\| \leqslant \|x - X_k\|, \ j \neq k\}, \tag{2}$$

for X_j being the nucleation site of C_j. VTs are the simplest, and most widely utilized, tessellation models as they are parametrized only by the nucleation sites X_j, which can be modeled by a spatial point process, of which the Poisson process is most commonly employed. Detailed treatment of VTs can be found in Refs. [3,54]. Drawbacks to VTs are that the cells are limited to convex polyhedra in $\mathbb{R}^3$ (i.e.

planar boundaries), and that the distributions of size and aspect ratios of the cells are significantly narrower than that observed in many polycrystalline materials. There are a vast number of VT variants which have been developed (e.g. multiplicatively weighted, k-order VTs, weighted VTs, additively weighted VTs, the Voronoi-G tessellation, etc.) [35], though only a few have been used in mechanics.

Beyond the VT, two additional tessellation models for polycrystalline representation are considered in this work. The first is the multiplicatively weighted VT [35, Chpt 3.1.1], which is a spherical growth model, abbreviated as SGT, and the second is an extension of the multiplicatively weighted VT, which is an ellipsoidal growth model, denoted as EGT. The SGT and EGT models are defined as

$$C_j = \{x \in \mathbb{R}^3 : T_j(x) \leqslant T_k(x), \forall j \neq k, \text{ s.t. } C_j \text{ is simply connected}\}. \tag{3}$$

The cell travel time $T_j(x)$ is the time it takes C_j to grow to x from its nucleation site X_j. For the SGT, $T_j(x) = \|x - X_j\|/v_j$ for v_j being the velocity of the growing cell, whereas $T_j(x) = \|x - X_j\|/v_j(\theta, \phi)$ for the EGT. The angles (θ, ϕ) are angles of a spherical coordinate system with respect to a local cartesian coordinate system per cell defining the ellipsoid semi-axes parameterized by Bunge–Euler angles $h = (\varphi'_1, \Phi', \varphi'_2)$. The cell velocity for the EGT is parametrized by the three axial directions of the ellipsoid $(v_{j_1}, v_{j_2}, v_{j_3})$ and the cell velocity in terms of θ, ϕ (dropping the subscript j) is

$$v(\theta, \phi) = \frac{v_1 v_2 v_3}{\sqrt{v_2^2 v_3^2 \sin^2(\phi) \cos^2(\theta) + v_1^2 v_3^2 \sin^2(\phi) \sin^2(\theta) + v_1^2 v_2^2 \cos^2(\phi)}}. \tag{4}$$

The models must also capture the crystallographic orientation per grain, which is parametrized by the Bunge–Euler angles $g = (\varphi_1, \Phi, \varphi_2)$. Thus, in summary: for each cell, the VT model is parametrized by $\{X_j, g_j\}$, the SGT model is parametrized by $\{X_j, v_j, g_j\}$, and the EGT model is parametrized by $\{X_j, v_{j_1}, v_{j_2}, v_{j_3}, h_j, g_j\}$ for $j = 1, 2, \ldots, N_C$, for N_C being the total number of grains. Modeling and simulating the parameters via an MPP random field model is addressed in Section 6. Prior to simulation, the parameter distributions are estimated by obtaining a best-fit realization of the tessellation models from 3D data, which leads to a comparison of tessellation model performance as discussed in the following sections.

3. Best-fit tessellation model to data

3D data sets of reconstructed microstructures obtained from experimental data collection techniques (e.g. EBSD-FIB serial sectioning) are slowly becoming more available [6]. These are very expensive and time consuming data sets to create, and virtual models from which so-called statistically equivalent microstructures are greatly motivated to study different instantiations of microstructure configurations. The intuitive approach to fit the tessellation models to data is to set the grain centroids as the nucleation sites and fit spheres and ellipsoids to the grains for the SGT and EGT models, respectively. For the SGT model, the realization of each grain velocity is estimated as $v_j = \sqrt[3]{3V_j/(4\pi)}$, for V_j being the grain volume. The best-fit ellipsoidal velocities and orientation per grain for the EGT model is obtained by equating the eigenvalues and eigenvectors of the grain's moment of inertia tensor to that of an ellipsoid. For example, the moment of inertia about the x_1-axis per grain with centroid $\bar{x}_j$ occupying N_j voxels with edge length Δ is computed as $I_{x_1 x_1} = \left(\sum_{n=1}^{N_j} \left(\left(x_{2_n} - \bar{x}_{2_j}\right)^2 + \left(x_{3_n} - \bar{x}_{3_j}\right)^2\right)\Delta^3\right) + N_j \Delta^4/12$, and the cross term with respect to the x_2-axis computed as $I_{x_1 x_2} = -\sum_{n=1}^{N_j} (x_{1_n} - \bar{x}_{1_j})(x_{2_n} - \bar{x}_{2_j})\Delta^3$. The eigenvectors of this
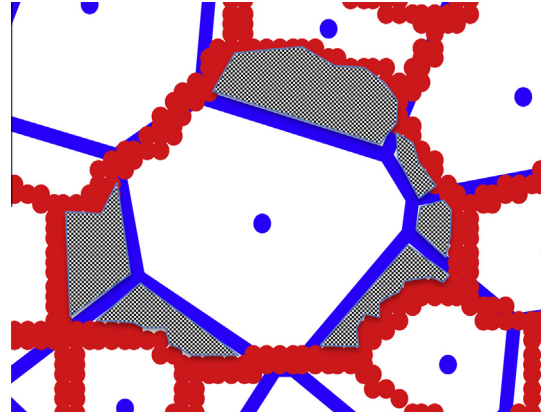

Fig. 1. Grain boundaries of reconstructed data in red and a VT in blue. The dark colored hatched region is the mismatch volume to be minimized. (For interpretation of the references to color in this figure legend, the reader is referred to the web version of this article.)

tensor form the local axis of the growing ellipsoid from which parameters $h_j = \left(\varphi'_{1_j}, \Phi'_j, \varphi'_{2_j}\right)$ are determined. The velocity components are determined by equating the eigenvalues $I_{1_j}, I_{2_j}, I_{3_j}$ to the moment of inertia terms of an ellipsoid and solving for the semi-axes components, for example $v_{1_j} = \sqrt{2.5(I_{2_j} + I_{3_j} - I_{1_j})/V_j}$. This approach for computing best-fit ellipsoids have been used in Refs. [7,17,44] and the only distinction here is that the velocity components of growing ellipsoids are determined rather than the semi-axes of ellipsoids.

These estimates of the best-fit parameters can be verified by minimizing the difference in grain boundary mismatch between the tessellation model and the data. Fig. 1 shows grain boundaries of the data in red and a VT in blue, and the hatched dark colored region is the mismatch volume per grain to be minimized.

The grain boundaries for the tessellation models are defined as the locations where growing neighboring grains first come in contact, and are found by equating the time that it takes neighboring grains to reach the boundary, that is

$$T_j(x) = T_k(x) \text{ for } x \in C_j \cap C_k. \tag{5}$$

Denote the set of boundary nodes intersecting grains C_j and C_k as $^{(k)}B^{(j)}$ for the microstructure data set. The travel time for grain C_j to reach boundary node $^{(k)}B_n^{(j)}$ for the VT model is $\frac{\|^{(k)}B_n^{(j)} - X_j\|}{v}$, since the cells are convex. Note that the VT model can be viewed as a growth model where all grains grow with identical velocity v. Thus for a given grain boundary node $^{(k)}B_n^{(j)}$, a measure of mismatch between the VT model and reconstructed microstructure is given as

$$f = \|^{(k)}B_n^{(j)} - X_j\| - \|^{(k)}B_n^{(j)} - X_k\|. \tag{6}$$

For the SGT and EGT model, the travel time argument is applied to develop a similar measure of grain mismatch. For the SGT model, this measure is given as

$$f = \frac{d_{jk} v_j}{v_j \cos(\beta_{j_n}) + v_k \cos(\beta_{k_n})} - d_{j_n}, \tag{7}$$

for $d_{jk} = \|X_j - X_k\|$, $d_{j_n} = \|X_j - {}^{(k)}B_n^{(j)}\|$, and β_{j_n}, β_{k_n} being the angle between $(X_j - X_k)$ and the line segments connecting X_j and X_k to $^{(k)}B_n^{(j)}$, respectively. Since the cells of the SGT and EGT models are not convex, the grain boundaries are not obtained by a linear travel path from the nucleation sites, and Eq. (7) is solved in an averaged sense. An objective function is obtained by squaring Eq. (7), averaging per grain boundary, and summing over all grain boundaries as

$$f = \frac{1}{^{(k)}N_B^{(j)}} \sum_{j=1}^{N_C} \sum_{k=1}^{N_N^{(j)}} \sum_{n=1}^{^{(k)}N_B^{(j)}} \left(\frac{d_{jk} v_j}{v_j \cos(\beta_{j_n}) + v_k \cos(\beta_{k_n})} - d_{j_n} \right)^2, \qquad (8)$$

for $^{(k)}N_B^{(j)}$ being the number of boundary nodes shared by grains C_j and C_k, $N_N^{(j)}$ being the number of neighbors of grain j. An equivalent objective function can be obtained for the EGT model by replacing v_j with $v(\theta, \phi)_j$ (see Eq. (4)). Such an optimization can be very expensive if the data set contains many grains. However, it is utilized in the example in Section 5.1 to verify that the estimated parameters of the SGT model give results nearly identical to the best attainable realization through Eq. (8).

4. Sample generation of growth models

For a given realization of parameters for a tessellation model, the associated sample virtual microstructure is generated in the following three steps. This procedure is preferred to growing the grains in the time domain because of the ease to which this process can be parallelized.

1. Voxel assignment to grains: The domain is voxelated and each voxel is assigned to the grain that takes the least time to reach the centroid, $\hat{x}$, of the voxel without interruption, that is $\min_j \left[\|X_j - \hat{x}\| / v(\theta, \phi)_j \right]$ for the EGT model and dropping the θ, ϕ dependence of grain velocity for the SGT model.
2. Ensure that every grain is simply connected: Since the voxel assignment in step 1 does not consider the intersection of growing grains, erroneous disconnected grain sets arise. The set of

simply connected grain voxels is obtained by first identifying the voxel containing the nucleation site of a grain and then iteratively identifying neighboring voxels that are assigned to the same grain. After no new voxels are identified, the disconnected voxels are the voxels assigned to the grain that have not been identified. These voxels are assigned to grains as per step 1 where all grains except grains previously assigned to the voxels compete. This process is repeated until all grains are simply connected.
3. Eliminate grains that are completely enclosed by another grain: The number of neighbors of each grain is counted. Grains that have one neighbor are eliminated and their voxels are reassigned to its neighbor.

Step 1 is equivalent to a point membership query with the predicate being a logical statement returning true for the grain reaching $\hat{x}$ first [48], while steps 2 and 3 are common operations in computer graphics to identify connected components and to fill voided volumes, respectively [21]. A sample microstructure of the EGT model consisting of $[189 \times 201 \times 117]$ voxels and 2353 grains takes approximately 8 min on a 1.7 GHz Intel Core i7 processor running a serial Fortran90 code, while the corresponding SGT model takes approximately 2 min.

5. Examples

5.1. 3D reconstructed nickel superalloy IN100

An Example 3D microstructure data set of a Nickel IN100 superalloy is freely available through the DREAM.3D open source
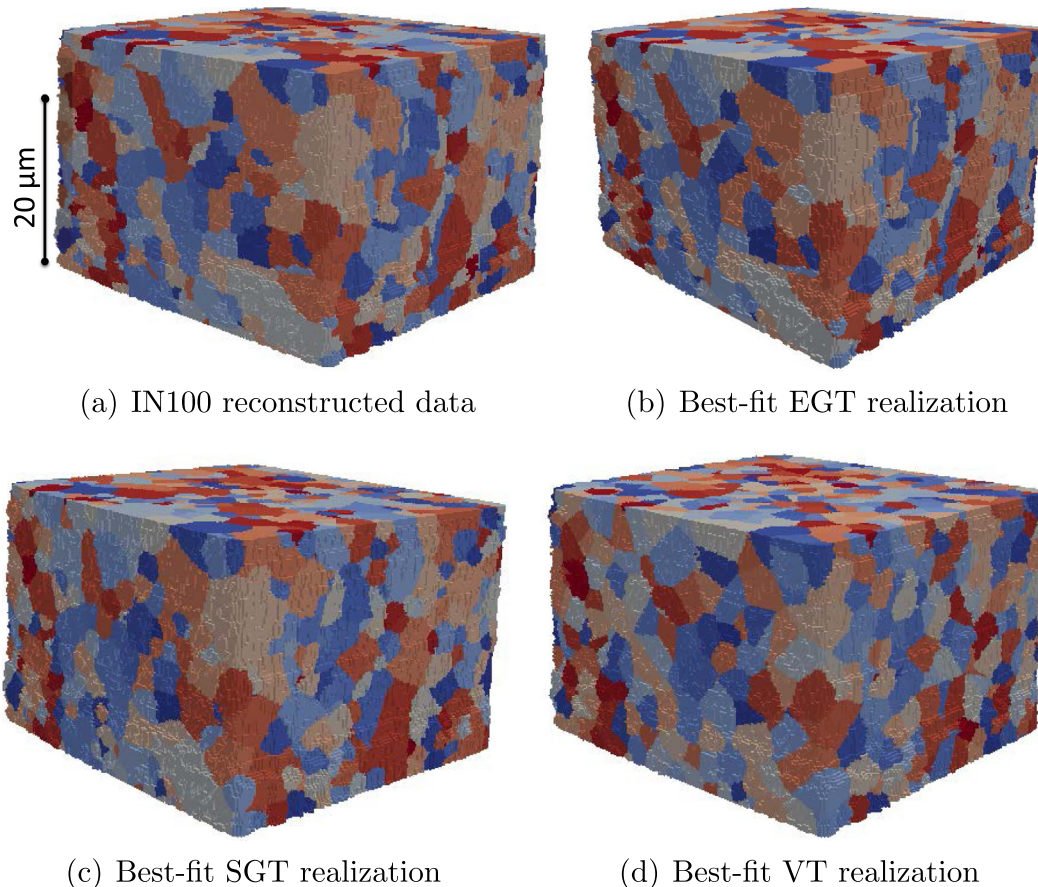

(a) IN100 reconstructed data

(b) Best-fit EGT realization

(c) Best-fit SGT realization

(d) Best-fit VT realization

Fig. 2. Reconstructed microstructure of IN100 Nickel superalloy data set along with best-fit realizations of tessellation models: (a) IN100 reconstructed data, (b) best-fit EGT realization, (c) best-fit SGT realization and (d) best-fit VT realization.
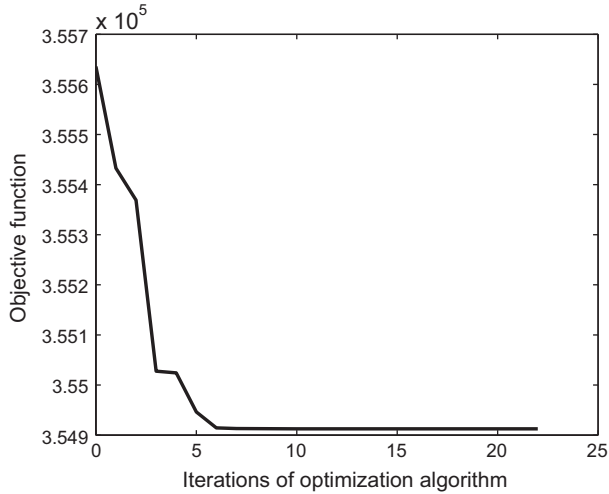
Fig. 3. Convergence of error function of Eq. (8) for SGT model parameters.

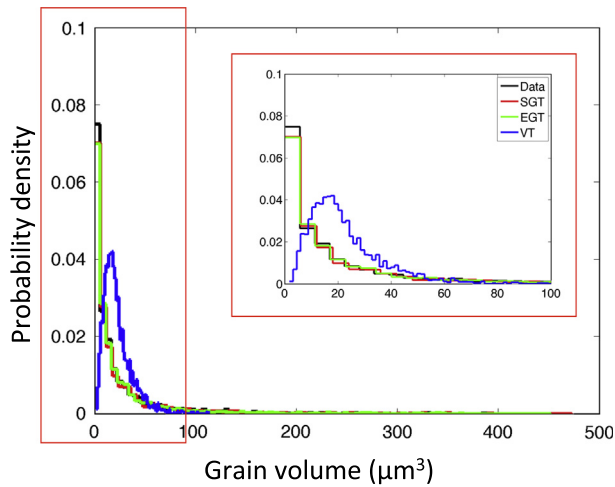Fig. 5. Empirical PMF of number of neighbors per grain.

Fig. 4. Empirical PDF of grain volume distribution.

software [18]. DREAM.3D facilitates the processing of digital microstructural data obtained from experimental data collection techniques (e.g. EBSD) by providing a large array of algorithms for segmenting, filtering, and quantifying microstructure features through a user-friendly interface. The example data set utilized is obtained using the default settings to reconstruct the IN100 sample and an image of it is shown in Fig. 2(a) alongside the best-fit reconstructed microstructures using the EGT (Fig. 2(b)), SGT (Fig. 2(c)), and VT (Fig. 2(d)) models. The voxel-based reconstructed microstructure data set consists of 2353 grains and is of size [189 × 201 × 117] with voxel edge length of .25 μm. The best-fit SGT and EGT models are obtained by finding equivalent spheres and ellipsoids as discussed in the beginning of Section 3, and the best-fit VT model is obtained by placing the nucleation sites at the centroids. By visually examining the morphology of the exposed grains in Fig. 2, it can be observed that the fit of the VT model is not very good, while the SGT and EGT models are significantly better. Quantitative measures of comparison are given below.

In order to check the accuracy of the best-fit SGT approximation in Section 3, the SGT model parameters are optimized according to Eq. (8) using the Trust-Region algorithm [8] as implemented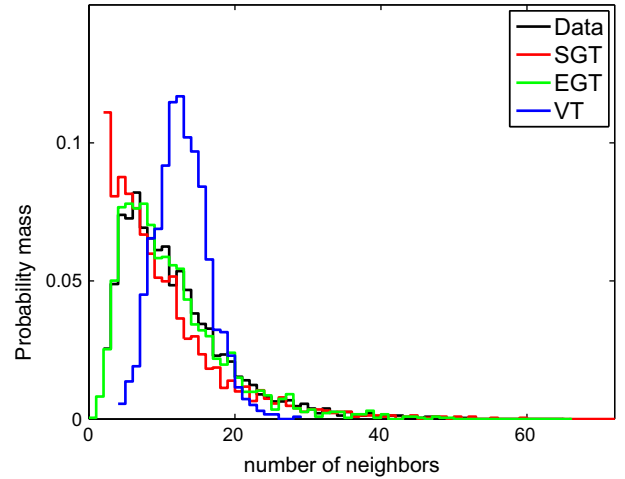 in MATLAB's FMINCON function, which is a gradient based optimization algorithm. The convergence of the optimization shown in Fig. 3, where the initial guess of the parameters corresponds to the best-fit approximation, took about 10 h on 1.7 GHz Intel Core i7 running serial MATLAB code. A negligible reduction in the objective function can be observed. One performance measure is the percent of mismatching voxels between the tessellations and the data (i.e. inconsistency of voxel assignment). The optimized SGT model has 17.5% inconsistency while the equivalent sphere SGT model has 17.59% inconsistency. This is compared to the EGT model with 9.99% inconsistency and the VT model having 51.15% inconsistency. Thus as the complexity of the models increase the performance increases significantly; it is worth emphasizing here the very large errors of the VT model.

5.2. Comparison of feature statistics

The performance of the tessellation models is assessed by graphical comparisons of empirically obtained probability distributions of microstructure features. The most commonly considered feature is grain size distribution, which is shown in Fig. 4. The SGT and EGT each perform well and do an excellent job in capturing the PDF for grain volumes greater than about 10 μm^3. Small grains are captured but the distribution of very small grains (< 10 μm^3) is slightly underrepresented. On the other hand, these tessellation models demonstrate an extremely significant improvement over the VT model, which severely misses both tails of the distribution (small grain and large grains) as well as the general shape.

Fig. 5 shows the distribution of number of neighbors per grain. This metric can be seen qualitatively as a low order metric regarding the boundary structure. The EGT model performs the best in capturing the shape of the probability mass function (PMF), while the SGT model overestimates the PMF for small number of neighbors. It can be seen graphically that the VT model appears to neither capture the mean or the variance of the PMF and it has a significantly different shape.

A metric for grain aspect ratio is typically obtained by finding the best-fit ellipsoid per grain and comparing the ratios of the 3 axes ($A \geqslant B \geqslant C$) of the ellipsoid. The best fit ellipsoid is obtained as discussed in Section 3. Empirical PDFs of $\frac{A}{B}$ and $\frac{A}{C}$ for the data and tessellation models are shown in Fig. 6(a) and (b), respectively. The EGT model shows significant improvement over the SGT and VT models in capturing the grain aspect ratio, while in this case VT outperforms SGT.

The distribution of the grain volume mismatch (i.e. volume of incorrectly assigned voxels) for all grains is given in Fig. 7.
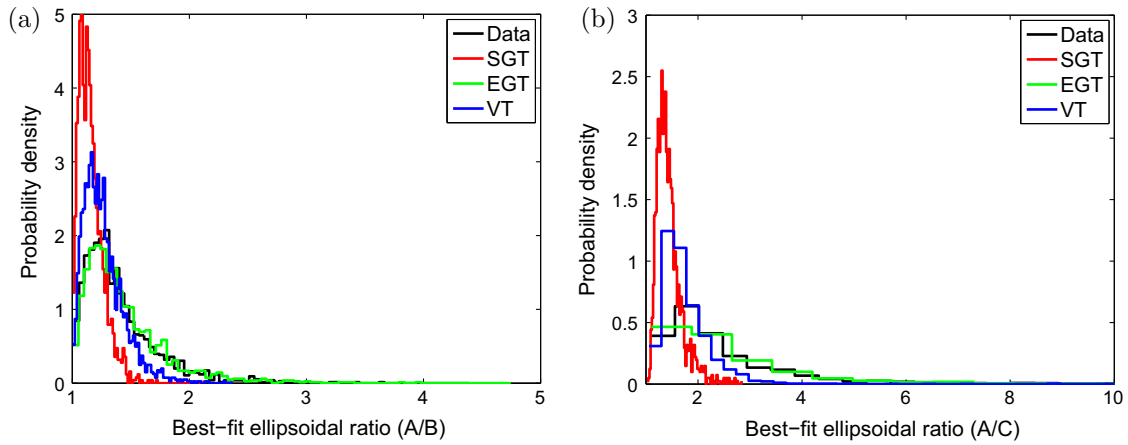
Fig. 6. Empirical PDFs of ratios of best-fit ellipsoid axes to quantify grain aspect ratio: (a) empirical PDF of best-fit ellipsoid ratio $\frac{A}{B}$ and (b) empirical PDF of best-fit ellipsoid ratio $\frac{A}{C}$.
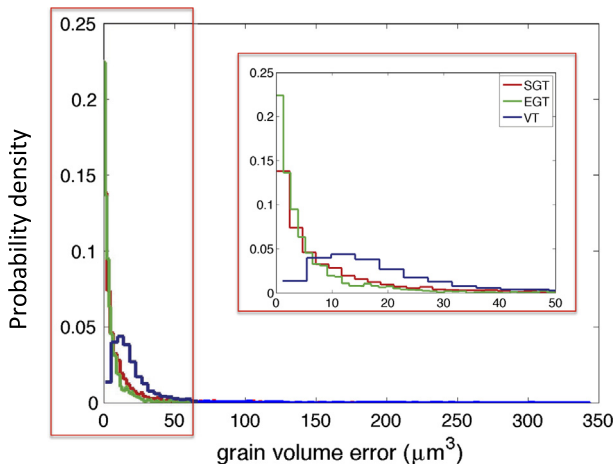

Fig. 7. Empirical PDF of grain volume error distribution.

A perfectly fitting model would have PDF equal to $\delta(x)$. The mismatch error between the SGT and EGT models are similar and are both much better than the VT model.

The Grain Boundary Character Distribution (GBCD), $\lambda(n, \Delta g)$, introduced in Ref. [42], is a quantitative measure of grain boundary types, and is defined as the relative area of boundaries as a function of surface normals with respect to crystallographic orientation of the grain n and the crystallographic misorientation Δg between the neighboring grains. Properties of the GBCD and methods to compute it are discussed in Refs. [42,44,46], and a GBCD analysis of the IN100 data set has been given in Ref. [41]. GBCDs for the data as well as the tessellation models were created through both the DREAM.3D software and the software provided in Ref. [40]. Voxel-based representations of the microstructures were input into DREAM.3D, and the grain boundaries were surface-meshed after undergoing a Laplacian smoothing process [11]. The surface mesh data (i.e. element area, normal direction, crystallographic
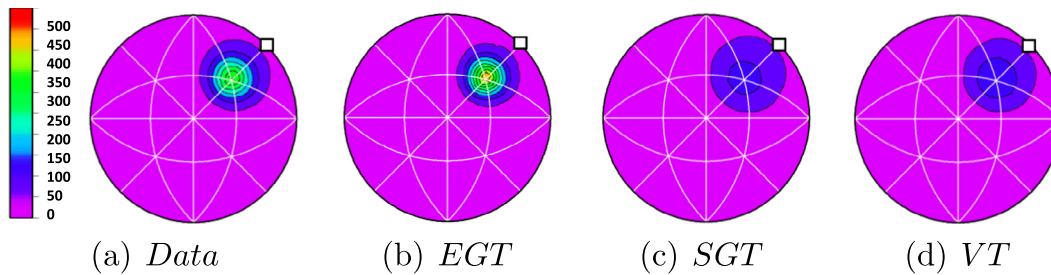

Fig. 8. Stereographic project of GBCD in [0 0 1] direction for misorientations given by $(1.0°, 1.0°, 1.0°, 60.0°)$ in axis-angle notation with units in MRD. The [1 1 0] direction is denoted by the square. The Miller indices refer to the direction of the grain boundary normals relative to the local crystallographic orientations: (a) Data, (b) EGT, (c) SGT and (d) VT.
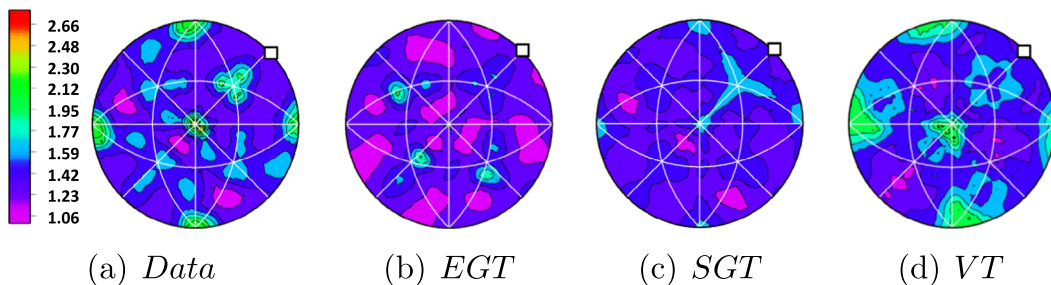

Fig. 9. Stereographic project of GBCD in [0 0 1] direction for misorientations given by $(1.0°, 1.0°, 1.0°, 5.0°)$ in axis-angle notation with units given in MRD. The [1 1 0] direction is denoted by the square. The Miller indices refer to the direction of the grain boundary normals relative to the local crystallographic orientations: (a) Data, (b) EGT, (c) SGT and (d) VT.
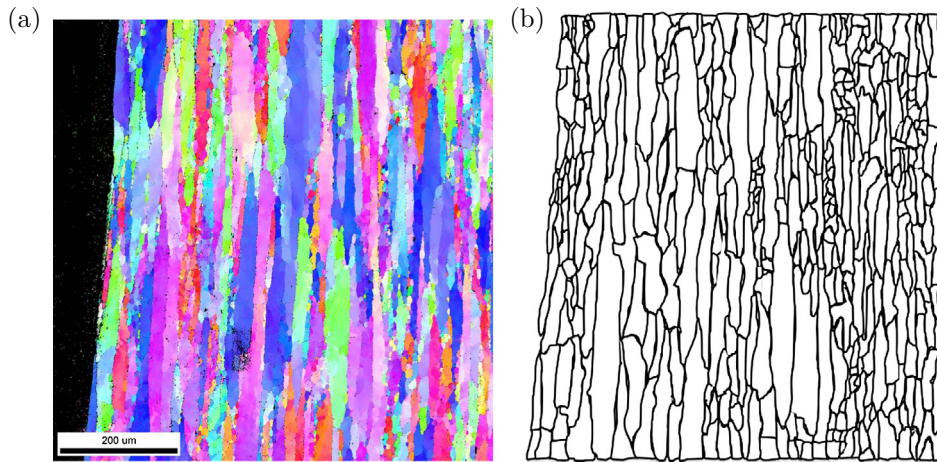
Fig. 10. EBSD micrograph of rolled aluminum alloy and its grain boundaries highlighted. Image courtesy of Dr. Dave Furrer of Pratt & Whitney: (a) EBSD micrograph and (b) grain boundary traces.

orientation of its adjacent neighbors) were outputted to create and visualize the GBCD from Ref. [40].

The GBCD is difficult to visualize because it is a function of 5 parameters so two snapshots are given. The stereographic projection on the $[0\,0\,1]$ direction for the data and the tessellation models for misorientation $(1.0°, 1.0°, 1.0°, 60.0°)$ using the axis-angle notation [12] is given in Fig. 8, and for misorientation $(1.0°, 1.0°, 1.0°, 5.0°)$ is given in Fig. 9. The Miller indices of the stereographic projection correspond to the direction of the grain boundary normals relative to the local crystallographic orientation.
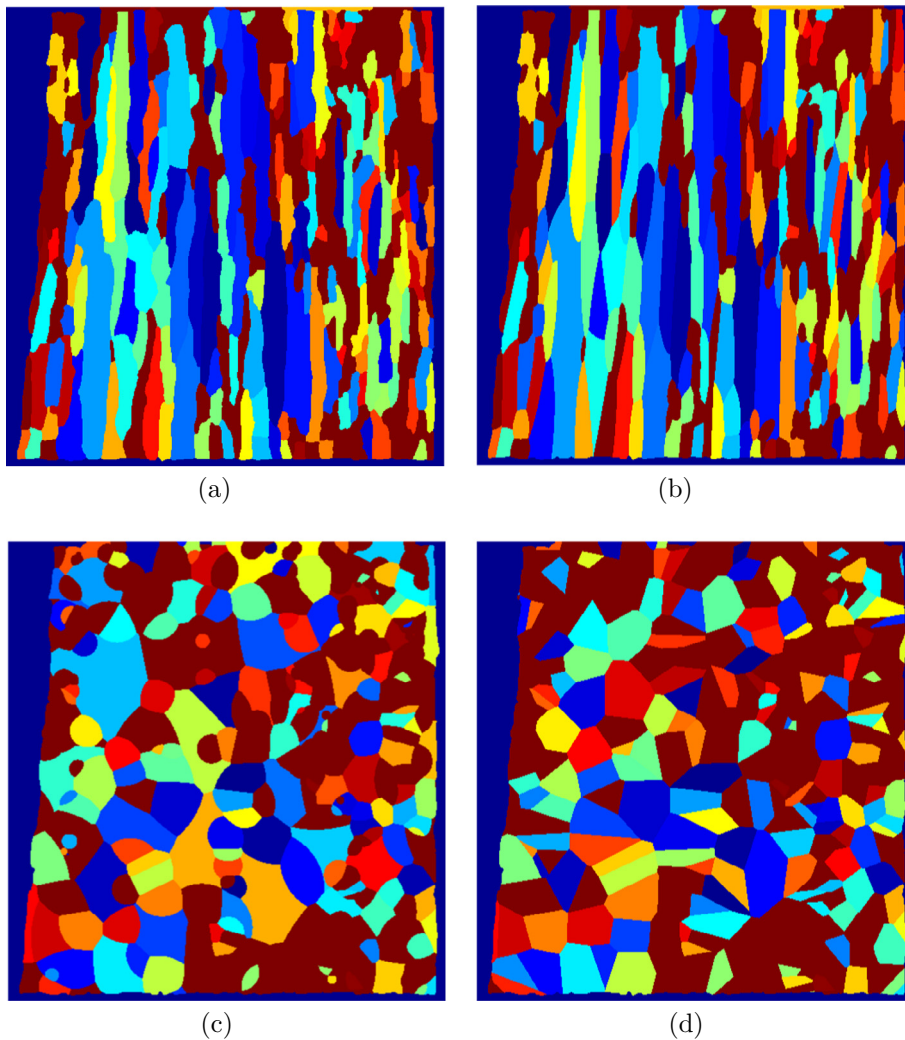

Fig. 11. Images of the rolled aluminum alloy along with best-fit tessellation models: (a) Data, (b) EGT, (c) SGT and (d) VT.
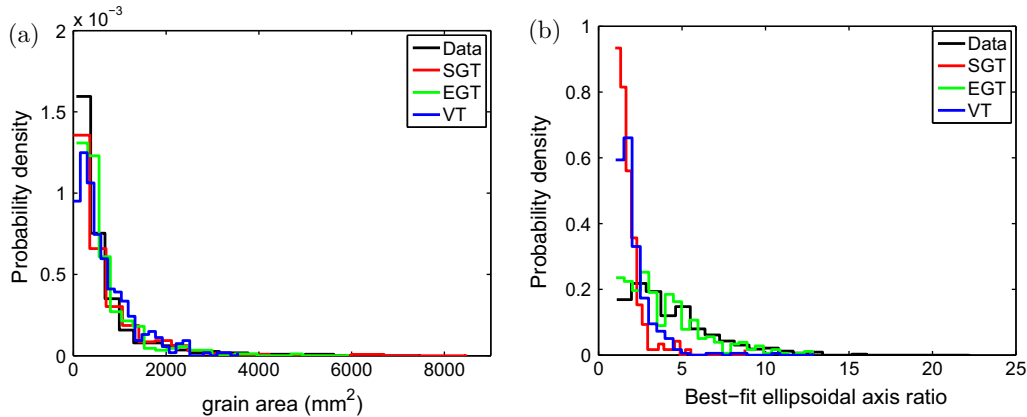
Fig. 12. Empirical PDF of the grain size and aspect ratio of the best-fit ellipse for the data and tessellation models in Fig. 11: (a) empirical PDF of grain size (mm^2) and (b) empirical PDF of best-fit ellipse aspect ratio.

The units of the GBCD are given in multiples of a random distribution (MRD), meaning that the GBCD is normalized with respect to that of a uniformly random distribution of internal grain surfaces [42]. Therefore, values greater than 1 imply a higher probability to occur than uniformly random and values less than 1 are less likely to occur. The large anisotropy of the GBCD in Fig. 8 illustrates the high density of $\Sigma3$ boundaries which corresponds to coherent twins. The EGT model is much better at capturing this boundary type than the other models. Fig. 9 shows a small-angle grain boundary (i.e. $\Sigma1$ boundary) that is closer to being uniformly random. Here, the models have values near that of the data but fail to capture the small fluctuations, as to be expected. A measure of the relative error is obtained by taking the ℓ^2-norm of the difference of the model GBCD with the data divided by the ℓ^2 norm of the data GBCD, and is given as .18, .53, and .48 for the EGT, SGT, and VT models, respectively. Note that for the tessellation models, the crystallographic orientation per grain is taken to be exactly that of the data; thus, discrepancies are due solely to morphological discrepancies. It is not expected that the GBCDs of the data and the models exactly match because that would indicate a perfect fit of the grain boundary morphology, but the results further demonstrate the significant improvement of the EGT model over the SGT and VT models.

5.3. 2D image of rolled aluminum alloy

This example demonstrates the extent to which the ellipsoidal growth model can capture oblique grains, such as those formed from hot rolling. An EBSD micrograph of a rolled aluminum alloy along with an image highlighting the grain borders, obtained from manual tracing of the image, is shown in Fig. 10.

Fig. 11 shows the best-fit realization of the tessellation models along with an image of the data plotted to the same scale. It can be observed that the EGT model captures the morphology fairly well while the SGT and VT models produce very poor results. Fig. 12 shows PDFs of the grain size and aspect ratio corroborating this observation.

6. Stochastic simulation of the EGT model for the 3D IN100 nickel alloy

This section describes the random field model chosen to simulate the EGT model according to the statistics obtained from the best-fit realization of the IN100 data set. The parameters of the EGT model conform to the MPP random field model [9,22,33]. An MPP is given as

$$Y = \{(\xi, m_\xi) : \xi \in \Xi, m_\xi \in M\}, \qquad (9)$$

for $\xi \in \mathbb{R}^3$ being a point in point process Ξ having associated mark (also known as intensity) m_ξ in sample space M. Detailed mathematical treatment and definitions of statistical measures can be found in [9, Chpt. 4]. The tessellation models studied have an additional complexity to traditional MPPs in that the marks are random vectors rather than scalar valued. In this context, ξ represents the locations of grain nucleation sites in the microstructure, and m_ξ are the grain parameters. For example, the EGT model marks are 9 dimensional random vectors given as

$$m_\xi = \left\{ v_1, v_2, v_3, (\varphi_1', \Phi', \varphi_2'), (\varphi_1, \Phi, \varphi_2) \right\}, \qquad (10)$$

where (v_1, v_2, v_3) are the three velocity components of the growing ellipsoid, $(\varphi_1', \Phi', \varphi_2')$ are the Euler angles of the ellipsoid orientation, and $(\varphi_1, \Phi, \varphi_2)$ are the Euler angles of the crystallographic orientation per grain.

There is no spatial dependence of the nucleation sites as well as dependence among the mark vectors for the IN100 example data set. This was determined by computing a covariance equal to zero among the mark vector components across grains, and complete spatial randomness of the nucleation sites as determined by the L-test [9, Chpt. 2.6]. However, there is dependence among the components within each mark vector and is addressed below. The hard core Matern process, which is an extension of the Poisson process such that no points are within a distance r of each other, is utilized to represent the nucleation sites. A mathematical description and simulation algorithm for the hard core Matern process is found in [9, Chpt 5.4]. The threshold minimum distance is due to the finite size of grains and the value $r = .3$ is used in the simulation. The homogeneous density of nucleation sites is estimated to be $\lambda = \frac{N_C}{|W|} = \frac{2353}{29.5 \times 47.25 \times 50.25} = .0339$. Had spatial correlation of the nucleation sites been observed, the interaction among the points can be modeled through the Markov point process class of models [33, Chpt. 6] and simulated through Markov Chain Monte Carlo methods.

Since the grain velocities are directly proportional to grain size, the distribution of the marks are dependent on the nucleation sites. The approach taken to simulate the MPP is to factor the joint distribution into the marginal distribution of the point process and the distribution of the marks conditioned on the point process, that is

$$f(\xi, m_\xi) = f(m_\xi | \xi) f(\xi). \qquad (11)$$

The point process is simulated first followed by the conditional distributions of the marks. There is significant flexibility in how to
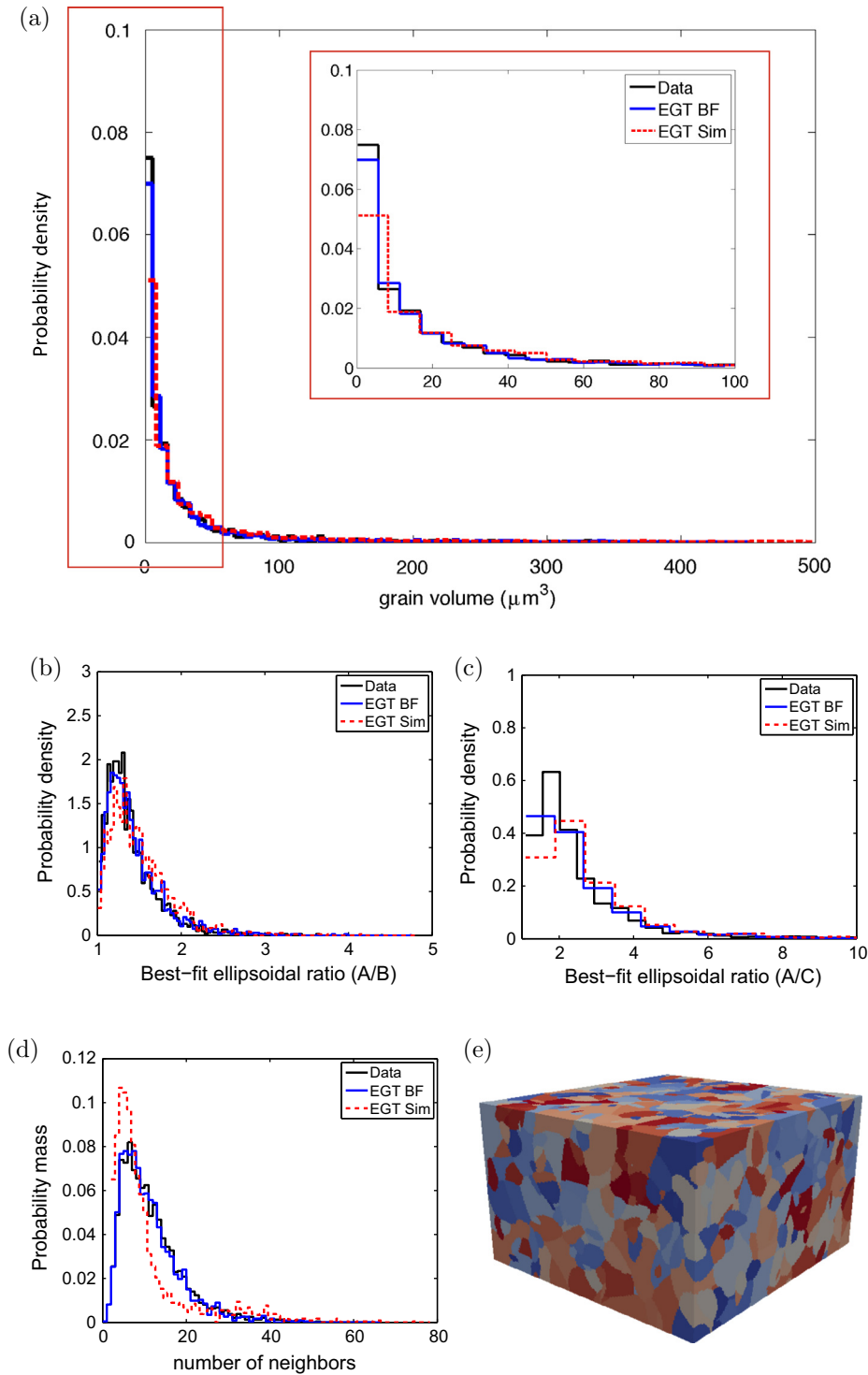
Fig. 13. Empirical PDFs morphological features and image of simulated EGT model: (a) grain size (μm^3) PDF, (b) best-fit ellipsoid ratio $\frac{A}{B}$ PDF, (c) best-fit ellipsoid ratio $\frac{A}{C}$ PDF, (d) number of neighbors per grain PMF and (e) realization of EGT model.

establish the conditional distributions of the marks from the best-fit tessellation sample. The approach taken is to divide the mark data into N_g groups, which are grouped according to the average distance of the closest N_n nucleation sites for a given mark. The group boundaries are determined such that all the groups have the same amount of data. For this example $N_g = 5$ is chosen because it is the largest number of groups to obtain sufficiently resolved empirical PDFs given the limited amount of data, and $N_n = 5$ because it is

heuristically determined to sufficiently identify the dependence of the marks on the nucleation site configuration.

The vector (intra-grain) components of the marks exhibit statistical dependence. The velocity components per grain are strongly correlated with an average correlation coefficient of .85. A negative correlation is observed between the Euler angles Φ' and φ_2' of the ellipsoid orientation having a correlation coefficient of $-.6$. All other parameter pairs have correlation coefficient smaller than

.1. The simulation of the mark components is done such that the marginal conditional distributions and associated correlation matrices obtained from data are matched. This is done by utilizing the Nataf transform and directly mapping the covariance matrix of the underlying multivariate Gaussian distribution $R_{0_{jk}}$ to the Spearman's rho of the marks through the analytical expression found in Ref. [29], details of which are given in Appendix A. This approach is also capable of capturing correlation of mark vector components across grains if it had been observed, and it has been implemented for simulating the three Euler angles defining crystallographic orientation in Ref. [34].

In order to test the accuracy of this form of the Nataf transform, 100,000 samples of the mark vector were generated for which empirical PDFs and covariance matrices were generated for each of the 5 conditional joint distributions (i.e. 45 marginal distributions and 5 9×9 covariance matrices). The difference between the target and simulated correlation matrix, $R_{j,k}$, for relative error metric given by $\sqrt{\sum_{j,k}(R_{j,k}^{\text{sim}} - R_{j,k}^{\text{target}})^2 / \sum_{j,k}(R_{j,k}^{\text{target}})^2}$ varies between .02 and .05. The marginal distributions obtained from simulation are essentially identical with those of the target, as to be expected. The error of the marginal PDFs of the mark vectors, $f(x)$, ranged from .0013 to .0125 for the relative error metric given as $\int \sqrt{(f_{\text{sim}}(x) - f_{\text{target}}(x))^2} dx / \int f_{\text{target}}(x) dx$.

Since simulating the hard core Matern process as well as random variables consistent with target marginal distributions and covariance matrices involve no optimization, sample realizations of the tessellation parameters can be generated almost instantaneously. The results of the generated microstructure samples are given below. Fig. 13 contains a realization (Fig. 13(e)) along with the grain size distribution (Fig. 13(a)), grain aspect ratios (Fig. 13(b) and (c)), and number of neighbors (Fig. 13(d)) compared with the best fit EGT and the data. In order to minimize sampling error, the densities in Fig. 13 were determined from 5 simulated microstructures each containing between 2400–3000 grains, and any incremental change in the empirical PDFs by generating new samples is negligible. There remain slight discrepancies between the distribution obtained from the best-fit realization and the simulations, such as under prediction of the probability of small grains and over prediction of grain sizes. The sources of these discrepancies, although difficult to quantify, are likely to be from simplifications in the random field model representation, parameter errors of the random field model due to limited data, and limitations of the simulation algorithm. Also, since the upper tail is associated with very low probabilities, it is likely that there is sampling error from the data set since only one microstructure sample is available. Overall, the results show that the microstructure features are captured very well by the simulation.

7. Conclusions

This work was motivated by the need for an accurate and efficient approach to simulate numerous instantiations of statistically equivalent polycrystalline microstructures. The methodology presented in this paper covers both the estimation of tessellation model parameters and the simulation of these parameters given a sample data set of a reconstructed microstructure. Through two examples, the ellipsoidal growth tessellation model was demonstrated to be accurate in capturing morphology features while having efficiency comparable to simple tessellation models (i.e. Voronoi tessellations). The marked point process is the proposed random field model to represent the tessellation parameters, which can be efficiently simulated using existing point process models conjoined with the Nataf transform for the marks.

Under the condition that a reconstructed microstructure data set is available, the approach proposed in this paper makes some significant contributions to the current state-of-the-art. It provides a quantitative means to evaluate the accuracy of a tessellation model by determining the best-fit sample to the data set (i.e. Section 3), and consequentially permits a performance comparison among competing models. The generation of statistically equivalent microstructures resorts to simulating the tessellation model parameters consistent with their statistics. The parsing of the parameters into a point process and multivariate distributions conditioned on the point process results in a tractable random field model to simulate. Accurately simulating the parameters ensures capturing the microstructure features of the best-fit sample. Therefore, the ability to capture more complicated correlations than that observed in the example data sets is promising, and this approach is likely to be better suited than optimizing a nonparametric model to match target distributions of microstructure features. Furthermore, this work introduces and demonstrates the reliability of a forward model to represent polycrystalline morphology, that being the ellipsoidal growth tessellation model. The value in having a forward model is that its parameters can be assigned arbitrary random field models in order to simulate hypothetical microstructures very rapidly, which could eventually become a useful tool in materials design. It is remarked that extensions to the model, such as inclusion of twins or multiphase subgrain morphology, remain to be implemented.

Ultimately, the performance of the tessellation models must be assessed by comparing the predicted mechanical response based on the virtual model and the 3D reconstructed data. Quantifying the uncertainty of micromechanical analysis requires quantifying discrepancies in predicted response between virtual models and reconstructed data as well as the variability in predicted response based on generating multiple realizations of microstructure morphology. The approach developed in this paper is a step towards improving the reliability of such predictions.

Appendix A

The Nataf transform is a composition of two transformations that map a random vector M with known marginal cumulative distribution functions (CDF) F_j and correlation matrix R_{jk} to a vector U comprised of independent standard normal random variables as $U = T_2 \circ T_1(M)$ where

$$T_1 : M \to Z = \begin{pmatrix} \Phi^{-1}(F_1(M_1)) \\ \Phi^{-1}(F_2(M_2)) \\ \vdots \\ \Phi^{-1}(F_N(M_N)) \end{pmatrix} \text{ and } T_2 : Z \to U = \Gamma Z, \tag{A.1}$$

where Z is a multivariate normal distribution with standard normal marginals and having covariance matrix $R_{0_{jk}}$, and Γ is a square root of R_0^{-1} typically obtained through the Cholesky factorization. The relationship between R_{jk} and $R_{0_{jk}}$ is

$$R_{jk} = \frac{1}{\sigma_j \sigma_k} \int \int_{\mathbb{R}^2} (F_j^{-1}\Phi(z_j) - \mu_j)(F_k^{-1}\Phi(z_k) - \mu_k)$$
$$\times \phi(z_j, z_k, R_{0_{jk}})dz_j dz_k, \quad\quad (A.2)$$

for μ_j being the mean value of M_j. Eq. (A.2) has no analytical solution and thus must be solved through optimization. However, an analytical expression relating the underlying covariance matrix R_0 and the Spearman's rho ρ_s of the target distribution exists and is given as

$$R_{0_{jk}} = 2 \sin\left(\frac{\pi}{6}\rho_s(M_j, M_k)\right). \quad\quad (A.3)$$

Through the analytical relationship of Eq. (A.3) the marks M can be simulated given that the underlying covariance matrix R_0 is positive definite (i.e. every marginal distribution and correlation structure cannot be captured by an underlying multivariate Gaussian, and it is necessary that R_0 is positive definite for such a mapping to exist).

References

[1] M. Anderson, D. Srolovitz, G. Grest, P. Sahni, Acta Metall. 32 (5) (1984) 783–791.
[2] S.R. Arwade, M. Grigoriu, J. Eng. Mech. 130 (9) (2004) 997–1005.
[3] F. Aurenhammer, ACM Comput. Surv. (CSUR) 23 (3) (1991) 345–405.
[4] F. Barbe, L. Decker, D. Jeulin, G. Cailletaud, Int. J. Plast. 17 (4) (2001) 513–536.
[5] I. Benedetti, M. Aliabadi, Comput. Mater. Sci. 67 (2013) 249–260.
[6] Y. Bhandari, S. Sarkar, M. Groeber, M. Uchic, D. Dimiduk, S. Ghosh, Comput. Mater. Sci. 41 (2) (2007) 222–235.
[7] A. Brahme, M. Alvi, D. Saylor, J. Fridy, A. Rollett, Scripta Mater. 55 (1) (2006) 75–80.
[8] R.H. Byrd, J.C. Gilbert, J. Nocedal, Math. Program. 89 (1) (2000) 149–185.
[9] S.N. Chiu, D. Stoyan, W.S. Kendall, J. Mecke, Stochastic Geometry and its Applications, John Wiley & Sons, 2013.
[10] J. Farjas, P. Roura, Acta Mater. 54 (20) (2006) 5573–5579.
[11] D.A. Field, Commun. Appl. Numer. Methods 4 (6) (1988) 709–712.
[12] F. Frank, Metall. Trans. A 19 (3) (1988) 403–408.
[13] D.T. Fullwood, S.R. Niezgoda, B.L. Adams, S.R. Kalidindi, Prog. Mater. Sci. 55 (6) (2010) 477–562.
[14] S. Ghosh, K. Lee, S. Moorthy, Int. J. Solids Struct. 32 (1) (1995) 27–62.
[15] L. Graham-Brady, X.F. Xu, J. Appl. Mech. 75 (6) (2008) 061001.
[16] M. Grigoriu, J. Appl. Phys. 94 (6) (2003) 3762–3770.
[17] M. Groeber, S. Ghosh, M.D. Uchic, D.M. Dimiduk, Acta Mater. 56 (6) (2008) 1257–1273.
[18] M.A. Groeber, M.A. Jackson, Integr. Mater. Manuf. Innov. 3 (1) (2014) 5.
[19] J. Guilleminot, A. Noshadravan, C. Soize, R. Ghanem, Comput. Methods Appl. Mech. Eng. 200 (17) (2011) 1637–1648.
[20] K. Hitti, P. Laure, T. Coupez, L. Silva, M. Bernacki, Comput. Mater. Sci. 61 (2012) 224–238.
[21] J.F. Hughes, S.K. Feiner, J.D. Foley, K. Akeley, M. McGuire, A.v. Dam, D.F. Sklar, Computer Graphics: Principles and Practice, Addison-Wesley Professional, 2013.
[22] J. Illian, A. Penttinen, H. Stoyan, D. Stoyan, Statistical Analysis and Modelling of Spatial Point Patterns, vol. 70, John Wiley & Sons, 2008.
[23] T. Kanit, S. Forest, I. Galliet, V. Mounoury, D. Jeulin, Int. J. Solids Struct. 40 (13) (2003) 3647–3679.
[24] Y.-T. Kim, N. Goldenfeld, J. Dantzig, Phys. Rev. E 62 (2) (2000) 2471.
[25] M. Knezevic, A. Levinson, R. Harris, R.K. Mishra, R.D. Doherty, S.R. Kalidindi, Acta Mater. 58 (19) (2010) 6230–6242.
[26] P.-S. Koutsourelakis, G. Deodatis, J. Eng. Mech. 131 (4) (2005) 397–412.
[27] K. Kumar, H. Van Swygenhoven, S. Suresh, Acta Mater. 51 (19) (2003) 5743–5774.
[28] C. Lautensack, S. Zuyev, Adv. Appl. Probab. (2008) 630–650.
[29] R. Lebrun, A. Dutfoy, Probab. Eng. Mech. 24 (2) (2009) 172–178.
[30] S. Li, A.A. Gazder, I.J. Beyerlein, E.V. Pereloma, C.H. Davies, Acta Mater. 54 (4) (2006) 1087–1100.
[31] J. Møller, Adv. Appl. Probab. (1989) 37–73.
[32] J. Møller, Adv. Appl. Probab. (1992) 814–844.
[33] J. Moller, R.P. Waagepetersen, Statistical Inference and Simulation for Spatial Point Processes, CRC Press, 2004.
[34] A. Noshadravan, R. Ghanem, J. Guilleminot, I. Atodaria, P. Peralta, Int. J. Uncertain. Quantificat. 3 (1) (2013).
[35] A. Okabe, B. Boots, K. Sugihara, S.N. Chiu, Spatial Tessellations: Concepts and Applications of Voronoi Diagrams, vol. 501, John Wiley & Sons, 2009.
[36] D. Raabe, Ann. Rev. Mater. Res. 32 (1) (2002) 53–76.
[37] D. Raabe, F. Roters, Int. J. Plast. 20 (3) (2004) 339–361.
[38] D. Raabe, M. Sachtleber, Z. Zhao, F. Roters, S. Zaefferer, Acta Mater. 49 (17) (2001) 3433–3441.
[39] C. Redenbach, I. Shklyar, H. Andrä, Int. J. Eng. Sci. 50 (1) (2012) 70–78.
[40] G. Rohrer. <http://mimp.materials.cmu.edu/gr20/stereology/>.
[41] G. Rohrer, J. Li, S. Lee, A. Rollett, M. Groeber, M. Uchic, Mater. Sci. Technol. 26 (6) (2010) 661–669.
[42] G.S. Rohrer, D.M. Saylor, B.E. Dasher, B.L. Adams, A.D. Rollett, P. Wynblatt, Z. Metallkd. 95 (4) (2004) 197–214.
[43] A. Rollett, D. Raabe, Comput. Mater. Sci. 21 (1) (2001) 69–78.
[44] D.M. Saylor, B.S. El Dasher, A.D. Rollett, G.S. Rohrer, Acta Mater. 52 (12) (2004) 3649–3655.
[45] D.M. Saylor, J. Fridy, B.S. El-Dasher, K.-Y. Jung, A.D. Rollett, Metall. Mater. Trans. A 35 (7) (2004) 1969–1979.
[46] D.M. Saylor, A. Morawiec, G.S. Rohrer, Acta Mater. 51 (13) (2003) 3663–3674.
[47] T.H. Scheike, Adv. Appl. Probab. (1994) 43–53.
[48] V. Shapiro, Handbook Comput. Aided Geom. Des. 20 (2002) 473–518.
[49] S.D. Sintay, M.A. Groeber, A.D. Rollett, 3D reconstruction of digital microstructures, in: Electron Backscatter Diffraction in Materials Science, Springer, 2009, pp. 139–153.
[50] R. Song, D. Ponge, D. Raabe, J. Speer, D. Matlock, Mater. Sci. Eng.: A 441 (1) (2006) 1–17.
[51] D.E. Spearot, K.I. Jacob, D.L. McDowell, Acta Mater. 53 (13) (2005) 3579–3589.
[52] L. St-Pierre, E. Héripré, M. Dexet, J. Crépin, G. Bertolino, N. Bilger, Int. J. Plast. 24 (9) (2008) 1516–1532.
[53] I. Steinbach, Modell. Simul. Mater. Sci. Eng. 17 (7) (2009) 073001.
[54] M. Tanemura, T. Ogawa, N. Ogita, J. Comput. Phys. 51 (2) (1983) 191–207.
[55] J.C. Tucker, L.H. Chan, G.S. Rohrer, M.A. Groeber, A.D. Rollett, Metall. Mater. Trans. A 43 (8) (2012) 2810–2822.
[56] C. Yeong, S. Torquato, Reconstructing random media, Phys. Rev. E 57 (1) (1998) 495.